

AlGa_N UV Detector with Largely Enhanced Heat Dissipation on Mo Substrate Enabled by van der Waals Epitaxy

Yang Chen, Hang Zang, Jianwei Ben, Shanli Zhang, Ke Jiang, Zhiming Shi, Yuping Jia, Mingrui Liu, Xiaojuan Sun,* and Dabing Li*



Cite This: *Cryst. Growth Des.* 2023, 23, 1162–1171



Read Online

ACCESS |



Metrics & More

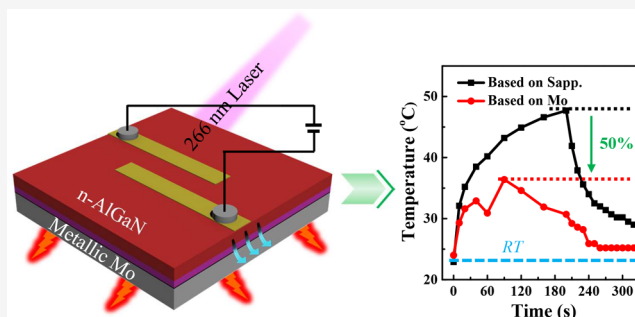


Article Recommendations



Supporting Information

ABSTRACT: The epitaxy of AlGa_N on metallic substrates exhibits numerous advantages including flexibility, vertical carrier injection, and enhanced heat dissipation for optoelectronic devices; however, there are still many challenges for the growth of AlGa_N according to the serious interfacial reaction and lattice mismatch by conventional epitaxial techniques. In this work, the *c*-oriented AlGa_N is grown on polycrystalline Mo substrate by van der Waals (vdWs) epitaxy with graphene as the insertion layer. A high-temperature annealed AlN is deposited as the nucleation layer, which optimizes the crystalline quality of following AlGa_N. The isolation effect of the graphene insertion layer results in a good epitaxial interface, which suppresses the atoms diffusion and chemical reaction, demonstrating by the theoretical calculation of high energy barriers for Al/Mo atoms penetrating through graphene insertion layer. The ultraviolet (UV) detector is fabricated by further growing a n-AlGa_N layer as the photosensitive absorber, whose responsivity ($1.7 \times 10^{-3} \text{ A W}^{-1}$) is comparable with that fabricated on conventional sapphire. Even better, the UV detector on the Mo substrate possesses enhanced heat dissipation ability due to its higher thermal conductivity, and the temperature elevation after consistently applying a drive voltage largely decreases by 50%. This work enlightens the growth of AlGa_N materials and fabrication of high-power/high-voltage optoelectronic devices on polycrystalline metallic substrates by the mean of vdWs epitaxy.



INTRODUCTION

The emerge of AlGa_N provides a promising material basis for the fabrication of optoelectronic devices working in the UV wavelength,^{1,2} as well as high-frequency and high-power electronic devices, benefiting from its adjustable wide bandgap, high electron mobility, and excellent stability at high voltage.³ Up to now, the epitaxy of AlGa_N is universally carried out on foreign substrates, including sapphire (Al₂O₃), silicon carbide (SiC), and (111) silicon (Si) due to the lack of high-quality homoepitaxial AlN template.^{4–6} Among these substrates, sapphire is widely used according to its appropriate cost, lower epitaxial difficulty, and feasible epitaxial crystalline quality. However, the poor thermal conductivity of sapphire (around $2 \text{ W K}^{-1} \text{ m}^{-1}$ at $200 \text{ }^\circ\text{C}$)⁷ results in heat accumulation in AlGa_N-based devices, especially for that working at high power and high voltage, inducing efficiency degradation or even failure.⁸

Metallic substrates, such as Mo, W, and Cu, have both of excellent thermal and electrical conductivity, for instance, around $131 \text{ W K}^{-1} \text{ m}^{-1}$ and $9.9 \times 10^{-3} \text{ } \Omega \text{ cm}$ for Mo at $200 \text{ }^\circ\text{C}$.⁹ Meanwhile, the natural ductility makes metallic substrates easily being extruded into thin foils with high flexibility. These advantages reveal that metals are more competitive as the

AlGa_N epitaxy substrates for the fabrication of flexible/wearable devices with vertical carrier injection and enhanced heat dissipation.^{10–12} However, the construction method by growth of AlGa_N on metallic substrates suffers from serious interfacial atoms diffusion and chemical reaction due to the high reactivity of metal in the rigorous epitaxial conditions, such as the high growth temperature (over $1000 \text{ }^\circ\text{C}$).¹³ Otherwise, the general polycrystalline nature of metallic substrates offers inconsistent epitaxial orientation,¹³ which causes chaotic crystal growth and poor crystalline quality in AlGa_N epilayers. A currently applied alternative strategy, including the laser-assisted epilayer lift-off, transfer, and bonding to metallic substrate, has avoided these difficulties mentioned above.^{14–16} Wang et al. recently presented the transfer of GaN epilayer from the sapphire onto Mo substrate, a 355 nm laser was used for GaN lift-off and the multilayer Ti–

Received: November 3, 2022

Revised: December 6, 2022

Published: December 23, 2022



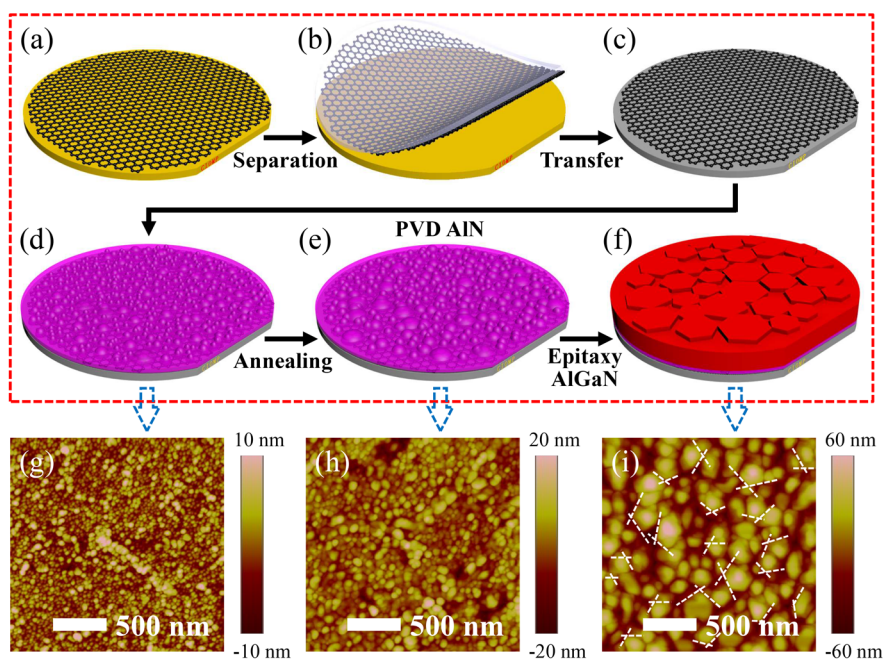


Figure 1. (a–c) Schematic diagram of the graphene transfer and (d–f) vdWs epitaxy of AlGaN on a 2-in. polycrystalline Mo wafer. A high-temperature annealed PVD AlN layer is prepared on graphene before the epitaxy of AlGaN by MOCVD. (g) AFM images of 200 nm PVD AlN on graphene, (h) after annealing at 1600 °C for 1 h, and (i) after epitaxy of AlGaN by MOCVD. The white dashed lines in (i) mark the hexagonal grain boundaries of AlGaN.

Pd–Ti composite was served as a bonding layer to the Mo substrate.¹⁵ However, it should be noted that the laser lift-off is usually time-consuming, and the generation of cracks is hardly avoided during the transfer and bonding processes. As for the AlGaN epilayer with higher Al content, the deep UV laser with much shorter excitation wavelength is essential for the lift-off,¹⁴ which is still restricted by the difficulty in obtaining high power density.

Two-dimensional (2D) materials, typical for graphene, h-BN, and transition metal disulfide compounds (e.g., MoS₂ and WSe₂), have the weak vdWs interaction in their interlayers. At the same time, the strong chemical bond of atoms in the plane makes excellent chemical and thermal stability for these 2D materials. The unique properties promote them severing as the insertion layers for the vdWs epitaxy of AlGaN-based materials.^{17–19} In this epitaxial configuration, the atomic 2D insertion layer could alleviate the matters caused by lattice mismatch and thermal expansion coefficient difference between the epilayer and heteroepitaxial substrate, which results in the enhanced crystalline quality and released residual stress.²⁰ Up to now, the vdWs epitaxy of AlGaN-based materials has been widely investigated on the single crystalline sapphire substrate, particularly, the AlN nucleation regulation and polarity control through the insertion of 2D materials have been reported in our previous works.^{17,21} Inspiring by the advantages of vdWs epitaxy, we consider that it is a promising strategy for the growth of AlGaN on polycrystalline metallic substrates, aiming at the easy fabrication of AlGaN-based optoelectronic devices. On the one hand, the impermeability for metal atoms through 2D materials would ensure the clear epitaxial interface by avoiding from interfacial atoms diffusion and chemical reaction; on the other hand, the remote epitaxial space at the interface screens the lattice field interaction of polycrystalline metals, potentially resulting in the single crystalline epitaxy of AlGaN.¹³

In present work, the growth of highly *c*-oriented AlGaN crystal and fabrication of UV detector with lateral metal-AlGaN-metal (M-AG-M) junctions on the polycrystalline Mo substrate are achieved by the vdWs epitaxy with a graphene insertion layer, and high-temperature annealed physical vapor deposition (PVD) AlN layer is first deposited on graphene for improving the AlGaN crystalline quality. The following AlGaN grown by metal organic chemical vapor deposition (MOCVD) has a high Al content of 92%, and the full width at half-maximum (fwhm) of rocking curve along (0002) orientation is 1.12°, which is much better than that grown without (w/o) graphene insertion layer. Meanwhile, the residual stress in epilayers decreases from 1.05 to 0.51 GPa. Thanks to the stability and impermeability of graphene insertion layer, the vdWs epitaxy ensures a clear and intact epitaxial interface between the epilayers and Mo substrate. The first-principles calculation proves that there are extremely high energy barriers for the Al and Mo atoms penetrating through the graphene, and thus, no serious interfacial atom diffusion and chemical reaction happen. The UV detector with n-AlGaN layer as the photosensitive absorber on the Mo substrate is fabricated, and a maximum responsivity of $1.7 \times 10^{-3} \text{ A W}^{-1}$ is achieved for it working at the wavelength of 266 nm, which is benefited from the well-arranged *c*-oriented AlGaN crystal, and the UV light detection ability is comparable with that on the sapphire substrate. Even better, the UV detector on the Mo exhibits enhanced heat dissipation ability after consistently applying a high drive voltage of 50 V, in which the elevation of device temperature largely decreases by 50% due to the higher thermal conductivity of Mo substrate, demonstrating the great potential for the future high-power/high-voltage optoelectronic devices with excellent thermal management capability.

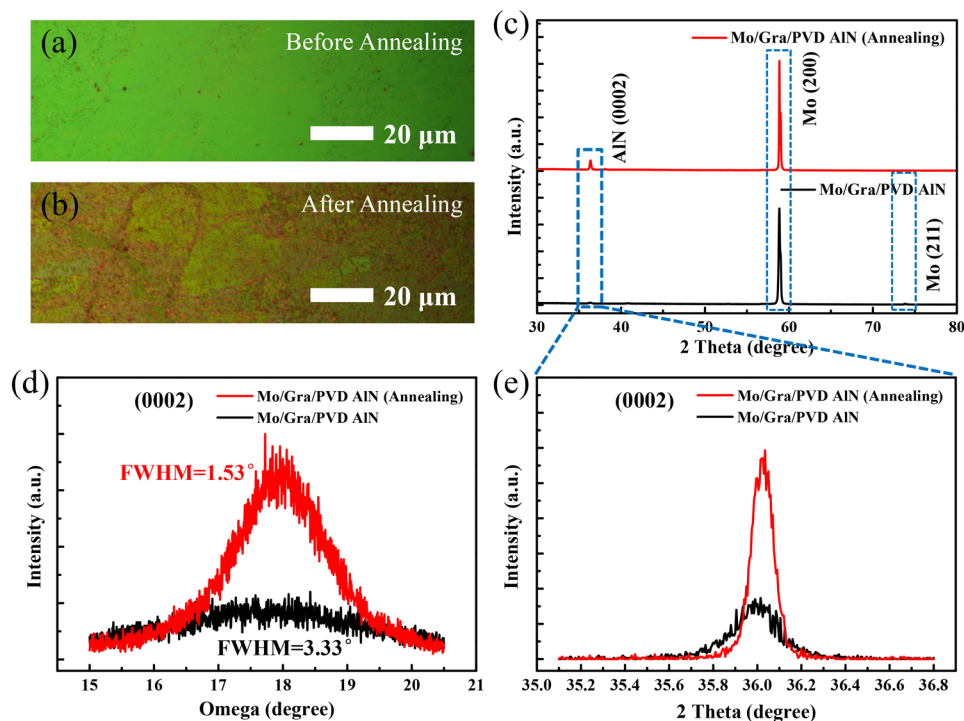


Figure 2. (a) OM images of PVD AlN on the Mo substrate before and (b) after the high-temperature annealing. (c) XRD 2θ and (d) rocking curve scan along (0002) orientation for the PVD AlN. (e) XRD fine-scanning for enlarged diffraction peak of PVD AlN, corresponding to that in (c).

RESULTS AND DISCUSSION

The growth of AlGa_N on metallic substrate is achieved by the vdWs epitaxy process, in which 2-in. polycrystalline Mo wafer with the coverage of graphene serves as the epitaxial substrate. As schematically shown in Figure 1a–c, the graphene is initially grown on catalytic Cu foils by chemical vapor deposition (CVD), then, it is transferred onto the Mo substrate by a polymer-assisted wet transfer method.²² The Raman spectra of graphene on the Mo is shown in Figure S1a, typical D, G, and 2D bands are observed. The weak intensity of D band proves less defects in graphene, and it has a monolayer nature according to the intensity ratio of 2D to G bands ($I_{2D}/I_G = 1.2$), this value is lower than the previously reported graphene transferred onto dielectric substrates (~ 2) due to the carrier doping of graphene by the Mo metal.^{23,24} In order to further confirm the layer number of graphene, it is transferred onto the dielectric sapphire, and the Raman spectra in Figure S1b shows an increased I_{2D}/I_G value of 2.49. The atomic force microscope (AFM) image of graphene on the Mo substrate shows several wrinkles, as marked by the white dashed lines, which might be generated during the growth and wet transfer processes, corresponding root-mean-square roughness (R_q) is 3.23 nm (see Figure S2). The X-ray diffraction (XRD) spectra of Mo is measured in Figure S3. Both of Mo (200) and Mo (211) crystalline planes are observed, implying its polycrystalline nature.²⁵

Before the vdWs epitaxy of AlGa_N, a 200 nm PVD AlN layer is initially deposited on the graphene insertion layer, serving as the nucleation layer, as shown in Figure 1d. After that, high-temperature (1600 °C) annealing is carried out to further enhance the crystalline quality of PVD AlN, as shown in Figure 1e. The AFM images of PVD AlN before and after annealing are shown in Figure 1g and h, respectively. To be different

from the selective nucleation of AlN on the defective wrinkles or broken boundaries of graphene by MOCVD in our previous work,²¹ the PVD AlN has the improved nucleation property with dense distribution on the graphene insertion layer. Furthermore, the size of AlN particles tends to be larger after the annealing process, which is attributed to the recrystallization of PVD AlN, suggesting the potentially enhanced AlN crystalline quality. Based on the annealed PVD AlN, the vdWs epitaxy of AlGa_N is carried out by MOCVD, as shown in Figure 1f and i. The AlGa_N exhibits hexagonal grains, as marked by the white dashed lines, corresponding to the typical *c*-oriented (0002) wurtzite crystal. The photography of samples at critical processing steps on a 2-in. Mo wafer is shown in Figure S4. The always mirror-liked reflection of Mo substrate after PVD AlN annealing and AlGa_N epitaxy imply that the graphene insertion layer ensures a clear and intact epitaxial interface.

The optical microscope (OM) images of PVD AlN before and after annealing are compared in Figure 2a and b. The surface morphology of PVD AlN becomes rougher after the high-temperature annealing, and it is consistent with the AFM results in Figure 1g and h, in which the R_q increases from 2.63 to 4.13 nm. The XRD 2θ scan in Figure 2c exhibits a single (0002) peak of wurtzite AlN, demonstrating a preferred *c*-oriented growth of AlN crystal. In addition, the XRD diffraction peaks of underneath polycrystalline Mo substrate could be simultaneously observed. The annealing process shows an effective impact on the diffraction intensity of PVD AlN along the (0002) orientation, as shown in Figure 2e of the XRD fine-scanning. The much higher diffraction intensity of PVD AlN after the annealing reveals an enhanced crystalline quality, which is further proved by the XRD rocking curve scan along (0002) orientation in Figure 2d, the fwhm of rocking curves decreases from 3.33° (before annealing) to 1.53° (after

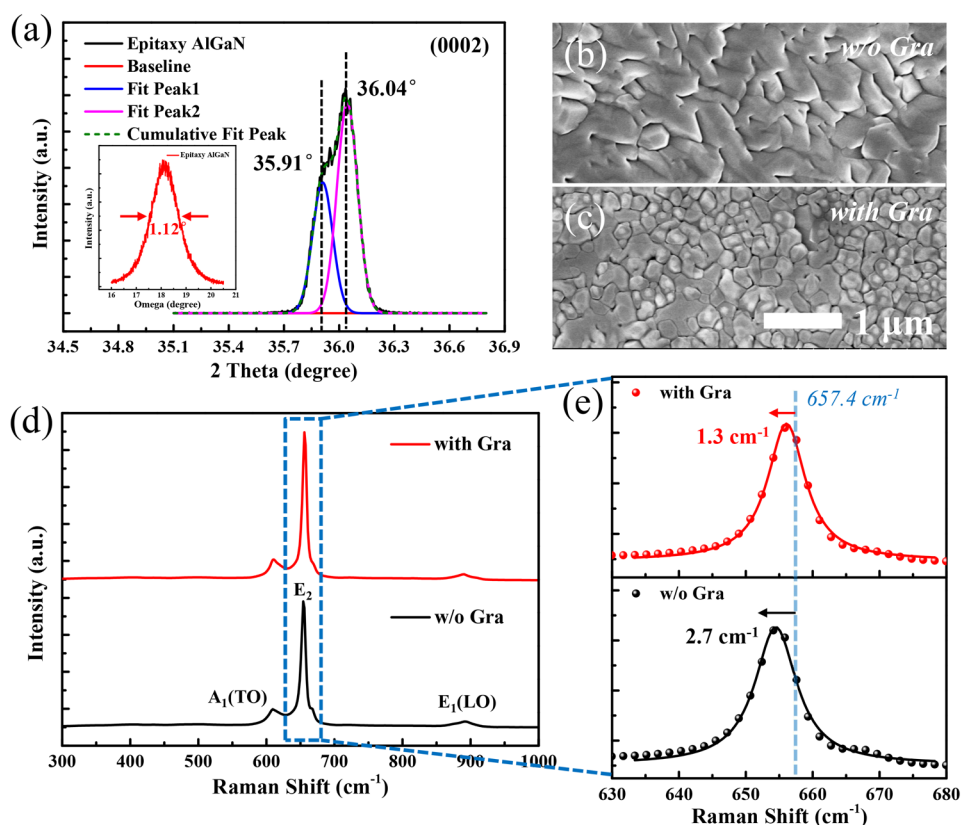


Figure 3. (a) XRD 2Theta scan along (0002) orientation for the vdWs epitaxy of AlGaN by MOCVD, and it is deconvoluted into two individual peaks with Gaussian type. Inset of (a) is the corresponding XRD rocking curve scan along (0002) orientation. (b) SEM images of AlGaN epilayer on the Mo substrate w/o and (c) with the graphene insertion layer. (d) Raman spectra of the epitaxial AlGaN. (e) Enlarged Raman E_2 band of AlGaN as the comparison with the stress-free one located at 657.4 cm^{-1} .

annealing). The optimization of PVD AlN crystalline quality by high-temperature annealing has been investigated in our previous work, proving that the formation of voids during the annealing process makes paired dislocations merging together, meanwhile, providing an inner surface for dislocation termination.²⁶

The vdWs epitaxy of AlGaN is further carried on the annealed PVD AlN by MOCVD, as the comparison, an identical annealed PVD AlN on bare Mo substrate w/o graphene insertion layer is provided. As shown in Figure 3a, the XRD 2Theta scan of AlGaN by vdWs epitaxy is deconvoluted into two individual peaks by “peak analyzer” package of Origin software, which locate at 35.91° and 36.04° , corresponding to the AlGaN with a high Al content of 92% and underneath AlN, respectively. The inset of Figure 3a is the XRD rocking curve scan of AlGaN along (0002) orientation, corresponding to a fwhm of 1.12° . The screw dislocation density is calculated as $\sim 3.22 \times 10^{10}\text{ cm}^{-2}$ according to the fwhm of rocking curve, implying an enhanced crystalline quality compared with the annealed PVD AlN in Figure 2d. Even better, the fwhm of AlGaN rocking curve also decreases in contrast to the early reported value (1.5°) in our previous work,¹³ demonstrating the excellent effect of PVD AlN annealing. As for the AlGaN epitaxy on the bare Mo substrate, its XRD diffraction intensity of 2Theta scan is extremely weak, both of the typical peaks belonged to AlGaN and AlN are difficult to be distinguished (see Figure S5). Even worse, the attempt of XRD rocking curve scan is failed because that none peaks could be detected. We consider that the direct contact of

PVD AlN with polycrystalline Mo substrate makes the chaotic crystalline orientations in the latter AlGaN epitaxy. In addition, the serious interfacial atoms diffusion and chemical reaction during high-temperature annealing is also responsible for the poor crystalline properties of epilayers.

The scanning electron microscope (SEM) images of AlGaN epitaxy on Mo substrate w/o and with the graphene insertion layer exhibit great difference in the grain arrangement and geometry, as compared in Figure 3b and c. Unlike the chaotic epitaxial orientation of AlGaN direct growth on the polycrystalline Mo substrate, the graphene insertion layer results in a *c*-oriented preferred grains, which tightly arrange together with a smoother surface morphology. These differences are further demonstrated by the AFM images in Figure S6, and the corresponding R_q decreasing from 30.2 to 23.6 nm. The surface morphology of AlGaN is related to their crystalline properties measured by XRD in Figures 3a and S5, implying that the graphene insertion layer could screen the lattice field interaction from the polycrystalline Mo substrate, thus, the vdWs epitaxy process is mainly controlled by the graphene insertion layer. The Raman spectra of AlGaN is shown in Figure 3d, typical $A_1(\text{TO})$, E_2 , and $E_1(\text{LO})$ bands are observed. It is known that the peak position of E_2 band reflects the residual stress in AlGaN epilayers. As shown in Figure 3e, the enlarged E_2 band of AlGaN is compared with the stress-free one, which locates at 657.4 cm^{-1} . The E_2 bands red-shift by 2.7 and 1.3 cm^{-1} for the AlGaN epilayer on Mo substrate w/o and with graphene insertion layer. The residual stress (σ) in epilayers could be calculated by the formula of

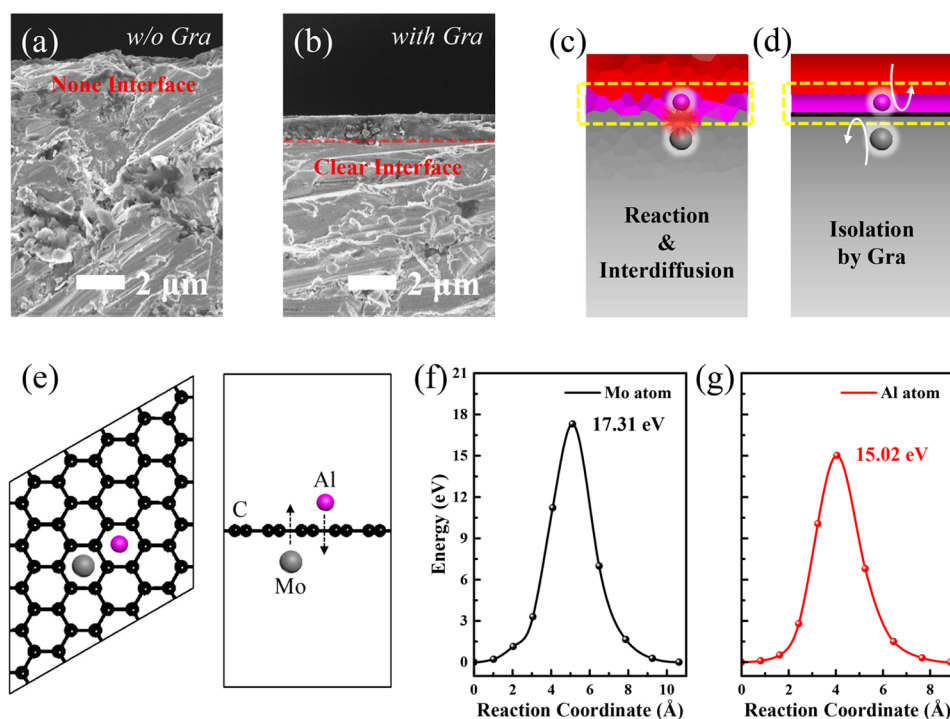


Figure 4. (a) Cross-sectional SEM images of AlGaIn epitaxy on Mo substrate w/o and (b) with graphene insertion. (c) Schematic diagrams of the interfacial atoms diffusion and chemical reaction of Al/Mo atoms w/o the graphene insertion layer, (d) intact and clear interface isolated by the graphene insertion layer. (e) Theoretical calculation models of the Mo/Al atoms penetrating through the graphene insertion layer. (f) Energy barrier distribution for Mo atom and (g) Al atom along the graphene insertion layer.

$\Delta E_2 = K \times \sigma$, and the ΔE_2 refers to the difference of E_2 band position with respect to the stress-free one, K is the stress coefficient of $\sim 2.56 \text{ cm}^{-1} \text{ GPa}^{-1}$.²⁷ By inserting a graphene layer, the residual stress in AlGaIn decreases from 1.05 to 0.51 GPa. As mentioned above, the graphene insertion layer makes the weak vdWs interaction between the AlGaIn and epitaxial substrate, and the residual stress induced by lattice distortion would be alleviated since the strong interfacial covalent bonding rarely happens.

The epitaxial interface morphology between the PVD AlN and Mo substrate is investigated by cross-sectional SEM, as shown in Figure 4a and b. The absence of graphene insertion layer makes the Mo metal blending together with the epitaxial materials, and none clear epitaxial interface is found in Figure 4a. As for the vdWs epitaxy, a clear and intact epitaxial interface appears with the graphene insertion layer, as marked by the red dashed line in Figure 4b. The total thickness of epilayers, including PVD AlN and epitaxial AlGaIn by MOCVD, is about $1.2 \mu\text{m}$. The corresponding epitaxial interface models are schematically compared in Figure 4c and d, respectively, showing that the graphene insertion layer has an important effect for achieving the clear and intact epitaxial interface. As for the absence of graphene insertion layer, the serious interfacial atoms diffusion and chemical reaction would happen during the high-temperature annealing of PVD AlN and epitaxy of AlGaIn, thus, resulting in the indistinguishable epitaxial interface, which are directly responsible for the degradation of crystalline quality. As shown in Figure 4d, these terrible situations could be suppressed by the interfacial isolation effect of graphene insertion layer. The theoretical calculations in Figure 4e–g demonstrates that the energies for both Mo and Al atoms penetrating through graphene insertion layer are extremely high, reaching up to 17.31 and 15.02 eV,

respectively.^{28,29} In other words, the insertion of graphene induces high energy barrier for atoms diffusion, therefore, the vdWs epitaxy process triggers the clear and intact epitaxial interface, which provides the prerequisites for the growth of c -oriented AlGaIn crystal.

The Mo atoms diffusion into the AlGaIn epilayers would also cause the dopant-induced higher electrical conductivity, otherwise, the blended epitaxial interface provides the path for current leakage passing through the underneath Mo substrate. For electrical properties measurement of epitaxial AlGaIn w/o and with the graphene insertion, we have fabricated the devices by depositing four In pads on their surface as contacts, and the device configurations are shown in Figure S7a and f, respectively. For each device, the current as a function of bias voltage is collected between each two adjacent In contacts of 1–2, 2–3, 3–4, and 4–1 with the bias voltage of -0.1 – 0.1 V, as plotted in Figure S7b–e and g–j, respectively. To be a well confirmation for the epitaxial interface conditions in Figure 4a–d, the epitaxy of AlGaIn on bare Mo substrate has a higher electrical conductivity, and the measured current rapidly increases with the bias voltage, which reaches to 10^{-2} – 10^{-1} A at 0.1 V. As the comparison, the current of AlGaIn vdWs epitaxy with graphene insertion layer is persistent at the order of magnitude in 10^{-6} – 10^{-4} A, and no dramatic current enhancement is observed along with the bias voltage increasing, well suggesting that limited atoms diffusion through the graphene insertion layer happens, and thus AlGaIn epilayers maintain a higher resistivity. It is well known that the high resistivity of AlGaIn is crucial for lowering the current leakage and ensuring the high performance of AlGaIn-based high-power/high-voltage electronics.

Based on the vdWs epitaxy of AlGaIn crystal on the Mo substrate, a conductive n -AlGaIn layer is further grown as the

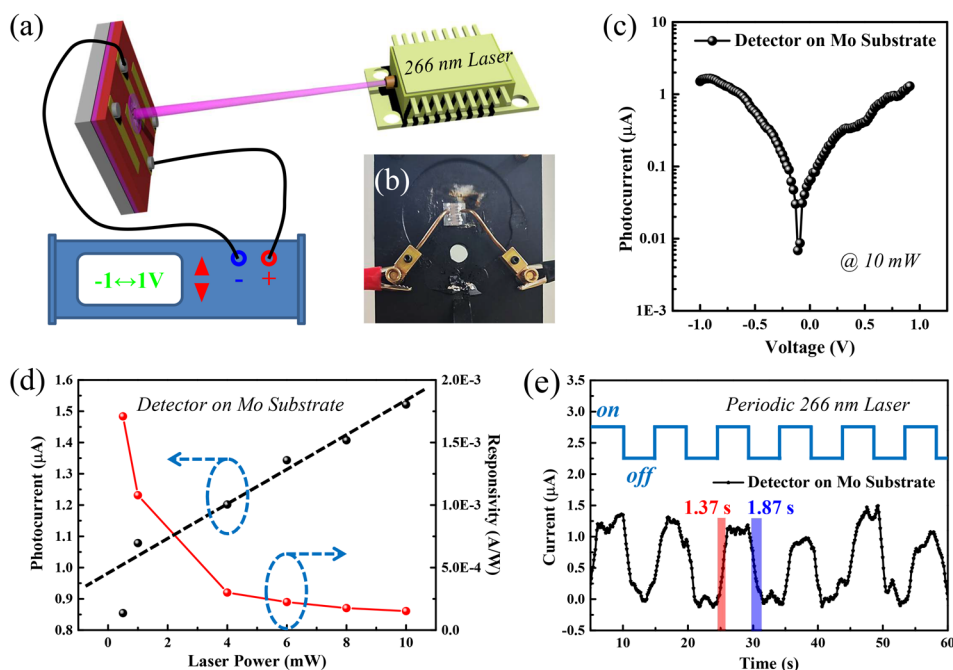


Figure 5. (a) Schematic diagrams of the measurement for the UV detector, and it has the lateral M–AG–M junctions. (b) Photography of UV detector fabricated on Mo substrate. (c) Photocurrent as a function of bias voltage and (d) laser power-dependent photocurrent and responsivity for the UV detector on Mo substrate. (e) Response time measurement by collecting the current with a periodic UV light irradiation.

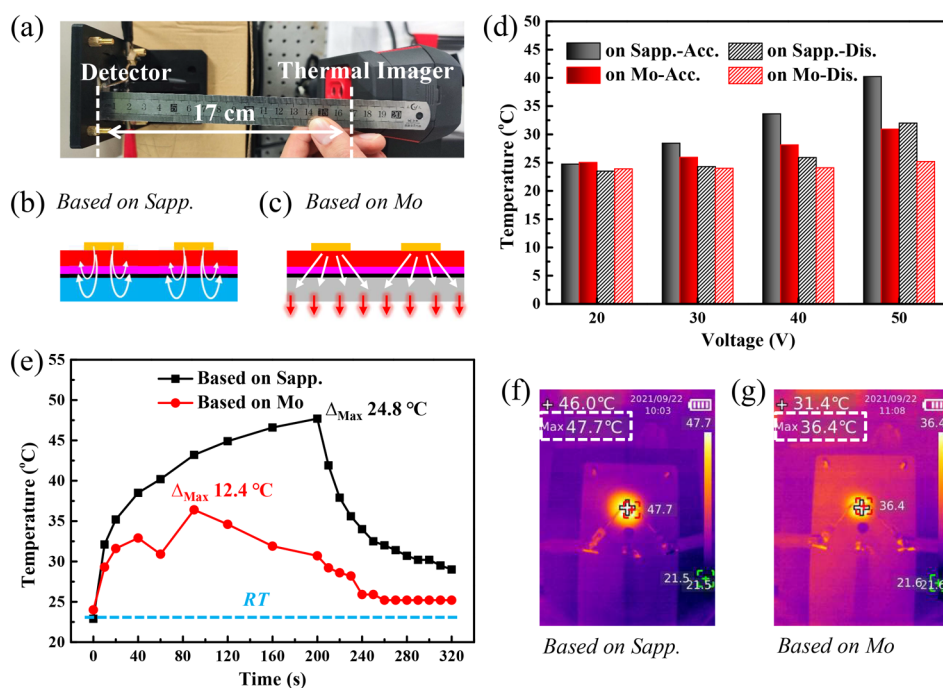


Figure 6. (a) Photography of the system for UV detector heat dissipation ability measurement. (b) Schematic diagram of the heat transportation in UV detector on the sapphire and (c) Mo substrates. (d) Heat Acc. and Dis. temperature as a function of drive voltage. (e) Time-dependent temperature variation: 0–200 s is under the drive voltage of 50 V, and 200–320 s removes the voltage. (f) Thermal imaging of the UV detector on sapphire and (g) Mo substrates at their maximum temperature.

photosensitive absorber for UV detector fabrication. After that, the interlaced Au strips are deposited onto n-AlGa_N as the electrodes for photocarriers collection, which forms the lateral M–AG–M junctions.³⁰ For the heat dissipation ability evaluation of UV detector on the Mo substrate in following sections, a device with identical structure is fabricated by the

vdWs epitaxy of AlGa_N on the conventional sapphire. The photoluminescence (PL) spectra of n-AlGa_N are measured at room temperature, the typical near-band-edge emission is observed at 326 and 313 nm for that on the Mo and sapphire substrates, as shown in Figure S8. The difference in the PL peak position reveals the Al content shift in n-AlGa_N (from

20% to 14%), which might be induced by the largely different thermal conductivity for these two substrates. The current of UV detector is collected at the bias voltage of -1 V, and a 266 nm laser is served as the UV light source. The schematic device structure and measured method are shown in Figure 5a. In Figure 5b, the photography of as-fabricated UV detector on the Mo substrate is shown in the center, and two probes contact on the Au electrodes for current collection.

The photocurrent (I_{ph}) of UV detector on the Mo substrate is plotted by calculating the difference in current measured at dark (I_{dark}) and 266 nm laser irradiation (I_{light}) conditions, as shown in Figure 5c. It obtains a typical photocurrent of 1.52 μ A at the bias voltage of -1 V, and the power of UV light is 10 mW. The detection ability to the UV light is also evaluated by changing the light power, and the variations of photocurrent and responsivity are plotted in Figure 5d. The responsivity (R) is calculated by the formula of $R = I_{ph}/P$, where P is the power of UV light irradiating on the n-AlGaIn absorber.^{30,31} The photocurrent near linearly increases with the UV light power, implying that the response is dominant by the excitation of photocarriers with incident photons.³² On the other hand, the responsivity tends to be saturated at higher light power, and a maximum responsivity of 1.7×10^{-3} A W⁻¹ is achieved at the laser power of 0.5 mW. As the light power increasing, the deduction in responsivity is attributed to the enhanced recombination between photogenerated carriers according to the reduced built-in electric field at the M-AG-M junctions, which is consistent with our early work.³¹ The response time is measured by irradiating the device with a periodic UV light source, whose frequency is ~ 0.2 Hz. The rise and fall time between 10% above the lowest current and 90% below the highest current are defined as the response (τ_{res}) time and recovery (τ_{rev}) time, thus, the typical τ_{res} and τ_{rev} are measured as 1.37 and 1.87 s, respectively. The τ_{res}/τ_{rev} of UV detector with n-AlGaIn photosensitive absorber are restricted by the trap states around Si dopant atoms, which result in the longer lifetime of photocarriers.³³ As shown in Figure S9, the photocurrent and response time of an identical UV detector on the sapphire are measured for comparison. It has a photocurrent of 3.36 μ A at the bias voltage of -1 V, and the τ_{res}/τ_{rev} is 2.4 s/0.85 s, which is on the same order of magnitude with that on the Mo substrate. The comparable device performance proves that the vdWs epitaxy provides a reliable method for the fabrication of AlGaIn-based photoelectronic devices on other metallic substrates.

It is known that the nonradiative recombination of carrier or current leakage would cause heat accumulation in photoelectronic devices, especially for it working at high drive voltage, which is correlated to the device working stability and lifetime. Therefore, the heat dissipation ability is one of key parameters to evaluate the performance of as-fabricated devices. Herein, a thermal imager is used to monitor the temperature of UV detector at various working conditions, including different drive voltage and working time, as shown in Figure 6a, and there is a distance of ~ 17 cm between the thermal imager and UV detector. The heat dissipation abilities of UV detector on the sapphire and Mo substrates are compared. The current as a function of drive voltage for the UV detector is plotted in Figure S10. The maximum current of 1.13 mA (on sapphire) and 1.36 mA (on Mo) is comparable, which indicates that the total thermal generation in n-AlGaIn layer should be similar. In this way, the maximum temperature of UV detector after the consistent voltage driving could

evaluate its heat dissipation ability. The temperature of UV detector as a function of drive voltage (20–50 V) is shown in Figure 6d. In this process, the device temperature is measured at 60 s after consistently driving by the voltage and another 60 s after removing the voltage, defining as the heat accumulation (Acc.) and dissipation (Dis.) steps, respectively. At the lower drive voltage of 20 V, the heat generation is not obvious, thus, the Acc. and Dis. temperature is closed to the room temperature (RT) of ~ 23 °C. As the drive voltage increasing, the temperature elevation of UV detector on Mo substrate alleviates in contrast to that on the sapphire, showing the largely enhanced heat dissipation ability according to the Acc. and Dis. temperature. Typically, the Acc. and Dis. temperatures decrease from 40.2 and 32 °C (on sapphire) to 30.9 and 25.2 °C (on Mo) at the drive voltage of 50 V. The heat dissipation enhancement of UV detector on the Mo as a comparison with that on the sapphire is summarized in Figure S11, clearly showing the largely enhanced heat dissipation for UV detector fabricated on the Mo at the drive voltage of 30–50 V.

The dynamic temperature variation as a function of working time is plotted in Figure 6e. At the first 200 s, the drive voltage maintains at 50 V, after that, the voltage is removed for later 120 s. The temperature of UV detector on the sapphire monotonously increases, reaching to the maximum difference (Δ_{Max}) of 24.8 °C at the time of 200 s, which is subtracted with the room temperature (~ 23 °C) at 0 s. However, the Δ_{Max} of 12.4 °C for that on Mo substrate emerges at the time of 90 s, and it is 50% lower than that on the sapphire. The corresponding thermal imaging at their maximum temperature is shown in Figure 6f and g. The difference in heat dissipation ability among the UV detector on sapphire and Mo substrates is illustrated by the heat transportation models in Figure 6b and c, respectively. Limiting by the poor thermal conductivity of sapphire, the heat generation at the UV detector is difficult to spread among the sapphire, then, it would be similarly hard for the following heat dissipation skipping the sapphire into the surrounding. As the result, the heat accumulation makes a larger temperature elevation in the UV detector, which is generally responsible for the device performance degradation. In contrast, the enhanced heat dissipation on metallic Mo substrate is attributed to its high thermal conductivity, thus, the thermal generation is immediately extracted into the surrounding. To be simplified, the Mo substrate has provided an efficient mediator for high throughput heat transportation. We consider that the excellent heat dissipation ability of UV detector on Mo substrate has demonstrated a novel strategy for the future fabrication of high-power/high-voltage optoelectronic devices via the easy vdWs epitaxy of AlGaIn on polycrystalline metallic substrates.

CONCLUSIONS

In conclusion, the growth of AlGaIn is achieved on the polycrystalline Mo substrate by the vdWs epitaxy process with the graphene as insertion layer, and the annealed PVD AlN serves as the nucleation layer, which optimizes the AlGaIn crystalline quality. Benefiting from the weak vdWs interaction of graphene insertion layer, the AlGaIn on Mo substrate has the preferred *c*-oriented growth and remission in residual stress. The first-principles calculation proves that there are large energy barriers for Mo and Al atoms penetrating through the graphene insertion layer, thus, the atoms diffusion and chemical reaction are suppressed. As the result, the clear and

intact epitaxial interface obtains the higher resistivity of AlGa_N epilayers, which is crucial for the fabrication of high-power/high-voltage electronics. The UV detector is fabricated on the Mo substrate by further epitaxy of n-AlGa_N layer as the photosensitive absorber. Despite the similar responsivity comparing with that on the conventional sapphire, the UV detector with lateral M–AG–M junctions on Mo substrate also possesses a largely enhanced heat dissipation ability, especially for it working at high drive voltage. This is attributed to the high thermal conductivity of Mo metal, which provides an unobstructed path for heat transportation. Present work demonstrates the strategy for growth of AlGa_N on polycrystalline metallic substrates via the vdWs epitaxy, enlightening the thoughts for easy design and fabrication high-power/high-voltage devices with higher working stability and longer lifetime.

METHODS

Epitaxial Substrates Preparation and Materials Growth.

Double side polished 2-in. Mo wafer with polycrystalline nature was purchased from a commercial company, and its thickness is 430 μm. The graphene was primarily grown on catalytic Cu foils by CVD, then, it was transferred onto the Mo wafer by a previously reported polymer-assisted wet transfer method,²² severing as the epitaxial substrates. Meanwhile, the graphene layer was simultaneously transferred onto a 2-in. sapphire substrate as the reference. A 200 nm AlN was first deposited on the epitaxial substrates as the nucleation layer by PVD. After that, the PVD AlN was annealed at 1600 °C for 1 h in the atmospheric pressure with N₂ protection.²⁶ Before the epitaxy of AlGa_N by MOCVD, a thin layer AlN and AlN/AlGa_N superlattice with 10 loops were deposited for higher crystalline quality (Figure S12 shows a XRD RC fwhm of 1.38° for epitaxy AlN, implying the enhanced crystalline quality of AlGa_N). The AlN was grown at 1250 °C with a V/III (NH₃/TMAl) of ~3, and the AlN/AlGa_N superlattice was grown at 1150 °C by alternant input of TMGa, whose flux was controlled at 20 sccm. For the undoped AlGa_N epitaxy, 20 sccm TMGa, 120 sccm TMAl, and 800 sccm NH₃ were injected, the growth temperature and chamber pressure were set as 1150 °C and 50 mbar. After the growth of 40 min, the thickness of undoped AlGa_N is about 350 nm. For later n-AlGa_N epitaxy, SiH₄ was served as the dopant, and the final thickness of n-AlGa_N is about 500 nm with a doping concentration of ~2 × 10¹⁸ cm⁻³, identifying by Hall measurement.

UV Detector Fabrication. The AlGa_N epilayers on 2-in. Mo wafer was cut into 1 × 1 cm² pieces by a tinsmith scissors, then, the cutting edges were polished by abrasive papers. As for the epitaxy of AlGa_N on sapphire substrate, it was separated via a laser beam cutting. For the resistivity measurement of undoped AlGa_N, four In pads were mechanically pressed onto the corners, and the adjacent In pads had a distance of 8 mm. After the epitaxy of n-AlGa_N, 30 nm Au strips were deposited through a certain patterned mask by electron beam deposition, and the Au electrodes had a space of 0.5 mm. In order to make the device more stable during the current collection, In pads were deposited onto Au electrodes for probes contact.

Theoretical Calculations. Density functional calculations were performed with the Perdew–Burke–Ernzerhof (PBE)³⁴ functional, and the projected augmented wave (PAW) plane-wave basis implemented in the Vienna ab initio simulation package (VASP)^{35,36} was used to describe the interaction between core and valence electrons.³⁷ The DFT–D3 correction was adopted for the van der Waals interaction. The transition state energy was calculated with the climbing image nudged elastic band (CI-NEB) method.³⁸ A 5 × 5 supercell of graphene with a 2 × 2 × 1 k-mesh was used to model the atom diffusion process. The spin polarization was considered for all the calculations. The energy cutoff for all the elements is 400 eV. The atomic structure relaxation was performed using the conjugate gradient scheme and the maximum force on each atom is set to be 0.02 eV Å⁻¹.

Materials Characterization and Device Measurement. The morphology of AlN nucleation layer and AlGa_N epilayers were evaluated by the OM (DS-Ri2, Nikon), SEM (S4800, Hitachi), and AFM (MULTIMODE 8, Bruker). The AFM worked in the tapping mode. The XRD (D8 Discover, Bruker) was used to measure the structural properties of Al(Ga)_N, and the parameters related to hexagonal crystal system of AlN were applied. The Raman spectrometer (LabRAM HR Evolution, HORIBA Scientific) was applied to identify the graphene properties and residual stress in the AlGa_N epilayer, and a 532 nm laser with 50% of its maximum power was used as the excitation source. The PL of n-AlGa_N was collected by a homemade system, and a 266 nm laser was applied for the near-band-edge emission of AlGa_N. The doping concentration of n-AlGa_N was confirmed by Hall measurement (8400 Series, TOYO). The current–voltage of undoped AlGa_N on metallic Mo was measured by a 2400 Source Meter, KEITHLEY. The current of UV detector with lateral M–AG–M junctions were also collected by the 2400 Source Meter, and a 266 nm laser (MPL-F-266-20 mW, CNI Laser) served as the light source. The applied bias voltage ranged from –1 to 1 V, and the laser power was calibrated at 0.5 mW, 1 mW, 4 mW, 6 mW, 8 mW, and 10 mW with a dynamometer. In order to obtain the periodic light input, an optical shutter was placed in front of the 266 nm laser. The temperature variation of UV detector driven by a consistent voltage was collected by a thermal imager (UTI220A Pro, UNI-T). There was a distance of ~17 cm between the thermal imager and target device.

ASSOCIATED CONTENT

Supporting Information

The Supporting Information is available free of charge at <https://pubs.acs.org/doi/10.1021/acs.cgd.2c01273>.

Raman spectra and AFM image of graphene, XRD spectra of Mo substrate, photography of as-prepared nitride materials, XRD spectra, AFM image, and current–voltage curves of AlGa_N, photoluminescence spectra of n-AlGa_N, performance of AlGa_N UV detector on sapphire substrate, current–voltage curves of AlGa_N UV detector, heat dissipation enhancement of UV detector, and XRD rocking curve of epitaxy AlN (PDF)

AUTHOR INFORMATION

Corresponding Authors

Xiaojuan Sun – State Key Laboratory of Luminescence and Applications, Changchun Institute of Optics, Fine Mechanics and Physics, Chinese Academy of Sciences, Changchun 130033, China; Center of Materials Science and Optoelectronics Engineering, University of Chinese Academy of Sciences, Beijing 100049, China; orcid.org/0000-0001-6836-3893; Email: sunxj@ciomp.ac.cn

Dabing Li – State Key Laboratory of Luminescence and Applications, Changchun Institute of Optics, Fine Mechanics and Physics, Chinese Academy of Sciences, Changchun 130033, China; Center of Materials Science and Optoelectronics Engineering, University of Chinese Academy of Sciences, Beijing 100049, China; orcid.org/0000-0001-5353-1460; Email: lidb@ciomp.ac.cn

Authors

Yang Chen – State Key Laboratory of Luminescence and Applications, Changchun Institute of Optics, Fine Mechanics and Physics, Chinese Academy of Sciences, Changchun 130033, China; Center of Materials Science and Optoelectronics Engineering, University of Chinese Academy of Sciences, Beijing 100049, China

Hang Zang – State Key Laboratory of Luminescence and Applications, Changchun Institute of Optics, Fine Mechanics and Physics, Chinese Academy of Sciences, Changchun 130033, China; Center of Materials Science and Optoelectronics Engineering, University of Chinese Academy of Sciences, Beijing 100049, China; orcid.org/0000-0002-1797-6857

Jianwei Ben – State Key Laboratory of Luminescence and Applications, Changchun Institute of Optics, Fine Mechanics and Physics, Chinese Academy of Sciences, Changchun 130033, China; Center of Materials Science and Optoelectronics Engineering, University of Chinese Academy of Sciences, Beijing 100049, China

Shanli Zhang – State Key Laboratory of Luminescence and Applications, Changchun Institute of Optics, Fine Mechanics and Physics, Chinese Academy of Sciences, Changchun 130033, China; Center of Materials Science and Optoelectronics Engineering, University of Chinese Academy of Sciences, Beijing 100049, China

Ke Jiang – State Key Laboratory of Luminescence and Applications, Changchun Institute of Optics, Fine Mechanics and Physics, Chinese Academy of Sciences, Changchun 130033, China; Center of Materials Science and Optoelectronics Engineering, University of Chinese Academy of Sciences, Beijing 100049, China

Zhiming Shi – State Key Laboratory of Luminescence and Applications, Changchun Institute of Optics, Fine Mechanics and Physics, Chinese Academy of Sciences, Changchun 130033, China; Center of Materials Science and Optoelectronics Engineering, University of Chinese Academy of Sciences, Beijing 100049, China; orcid.org/0000-0002-1207-570X

Yuping Jia – State Key Laboratory of Luminescence and Applications, Changchun Institute of Optics, Fine Mechanics and Physics, Chinese Academy of Sciences, Changchun 130033, China; Center of Materials Science and Optoelectronics Engineering, University of Chinese Academy of Sciences, Beijing 100049, China

Mingrui Liu – State Key Laboratory of Luminescence and Applications, Changchun Institute of Optics, Fine Mechanics and Physics, Chinese Academy of Sciences, Changchun 130033, China; Center of Materials Science and Optoelectronics Engineering, University of Chinese Academy of Sciences, Beijing 100049, China

Complete contact information is available at:
<https://pubs.acs.org/10.1021/acs.cgd.2c01273>

Author Contributions

Y. Chen carried out the Raman, XRD, AFM, SEM, PL measurements; transferred the graphene film; fabricated the UV detector and tested its performance; and wrote the manuscript. H. Zang performed the theoretical calculations and analyzed the theoretical results. J. W. Ben performed the growth and annealing of PVD AlN. S. L. Zhang performed the growth of AlGaIn epilayers by MOCVD. Z. M. Shi provided the theoretical calculation method and supervised the theoretical results. K. Jiang, Y. P. Jia, and M. R. Liu helped in the experimental data processing and result discussion. X. J. Sun and D. B. Li designed the whole study; supervised the project; and revised the manuscript.

Notes

The authors declare no competing financial interest.

ACKNOWLEDGMENTS

This work was supported by the National Key R&D Program of China (2021YFA0715600, 2021YFB3601600), National Natural Science Foundation of China (52002368, 61922078, 62121005, 61827813, 61874118, 62074147), Youth Innovation Promotion Association of the Chinese Academy of Sciences (Y201945, 2019222), Key Research Program of Frontier Sciences, Chinese Academy of Sciences (ZDBS-LY-JSC026), Key Research Program of the Chinese Academy of Sciences (XDPB22), and the Key-Area Research and Development Program of Guangdong Province (2020B010169001).

REFERENCES

- (1) Li, D. B.; Jiang, K.; Sun, X. J.; Guo, C. L. AlGaIn Photonics: Recent Advances in Materials and Ultraviolet Devices. *Adv. Opt. Photonics* **2018**, *10*, 43–110.
- (2) Amano, H.; Collazo, R.; Santi, C. D.; Einfeldt, S.; Funato, M.; Glaab, J.; Hagedorn, S.; Hirano, A.; Hirayama, H.; Ishii, R.; Kashima, Y.; Kawakami, Y.; Kirste, R.; Kneissl, M.; Martin, R.; Mehnke, F.; Meneghini, M.; Ougazzaden, A.; Parbrook, P. J.; Rajan, S.; Reddy, P.; Römer, F.; Ruschel, J.; Sarkar, B.; Scholz, F.; Schowalter, L. J.; Shields, P.; Sitar, Z.; Sulmoni, L.; Wang, T.; Wernicke, T.; Weyers, M.; Witzigmann, B.; Wu, Y.-R.; Wunderer, T.; Zhang, Y. W. The 2020 UV emitter roadmap. *J. Phys. D Appl. Phys.* **2020**, *53*, 503001.
- (3) Roccaforte, F.; Greco, G.; Fiorenza, P.; Iucolano, F. An Overview of Normally-Off GaN-Based High Electron Mobility Transistors. *Materials* **2019**, *12*, 1599.
- (4) Nagasawa, Y.; Hirano, A. A. Review of AlGaIn-Based Deep-Ultraviolet Light-Emitting Diodes on Sapphire. *Appl. Sci.* **2018**, *8*, 1264.
- (5) SaifAddin, B. K.; Almogbel, A. S.; Zollner, C. J.; Wu, F.; Bonef, B.; Iza, M.; Nakamura, S.; DenBaars, S. P.; Speck, J. S. AlGaIn Deep-Ultraviolet Light-Emitting Diodes Grown on SiC Substrates. *ACS Photonics* **2020**, *7*, 554–561.
- (6) Sun, Y.; Zhou, K.; Feng, M. X.; Li, Z. C.; Zhou, Y.; Sun, Q.; Liu, J. P.; Zhang, L. Q.; Li, D. Y.; Sun, X. J.; Li, D. B.; Zhang, S. M.; Ikeda, M.; Yang, H. Room-temperature continuous-wave electrically pumped InGaIn quantum well blue laser diode directly grown on Si. *Light Sci. Appl.* **2018**, *7*, 13.
- (7) Lee, S.-M.; Choi, W.; Kim, J.; Kim, T.; Lee, J.; Im, S. Y.; Kwon, J. Y.; Seo, S.; Shin, M.; Moon, S. E. Thermal Conductivity and Thermal Boundary Resistances of ALD Al₂O₃ Films on Si and Sapphire. *Int. J. Thermophys* **2017**, *38*, 176.
- (8) Ruschel, J.; Glaab, J.; Beidoun, B.; Ploch, N. L.; Rass, J.; Kolbe, T.; Knauer, A.; Weyers, M.; Einfeldt, S.; Kneissl, M. Current-induced degradation and lifetime prediction of 310 nm ultraviolet light-emitting diodes. *Photonics Res.* **2019**, *7*, B36–40.
- (9) Tye, R. P. Preliminary measurements on the thermal and electrical conductivities of molybdenum, niobium, tantalum and tungsten. *J. Less-Common Met.* **1961**, *3*, 13–18.
- (10) Chung, K.; Lee, K.; Tchoe, Y.; Oh, H.; Park, J. B.; Hyun, J. K.; Yi, G.-C. GaIn microstructure light-emitting diodes directly fabricated on tungsten-metal electrodes using a micro-patterned graphene interlayer. *Nano Energy* **2019**, *60*, 82–86.
- (11) Zhao, M. L.; Tang, X. S.; Huo, W. X.; Han, L. L.; Deng, Z.; Jiang, Y.; Wang, W. X.; Chen, H.; Du, C. H.; Jia, H. Q. Characteristics of AlGaIn/GaN high electron mobility transistors on metallic substrate. *Chin. Phys. B* **2020**, *29*, 048104.
- (12) Hiroki, M.; Kumakura, K.; Yamamoto, H. Enhancement of performance of AlGaIn/GaN high electron-mobility transistors by transfer from sapphire to a copper plate. *Jpn. J. Appl. Phys.* **2016**, *55*, 05FH07.
- (13) Chen, Y.; Zang, H.; Zhang, S. L.; Shi, Z. M.; Ben, J. W.; Jiang, K.; Jia, Y. P.; Liu, M. R.; Li, D. B.; Sun, X. J. Van der Waals Epitaxy of c-Oriented Wurtzite AlGaIn on Polycrystalline Mo Substrates for Enhanced Heat Dissipation. *ACS Appl. Mater. Interfaces* **2022**, *14*, 37947–37957.

- (14) Zhang, X. Y.; Ruan, Y. J.; Chen, S. Y.; Li, C. GaN/metal/Si heterostructure fabricated by metal bonding and laser lift-off. *J. Semicond.* **2009**, *30*, 123001.
- (15) Wang, Q.; Liang, Z. W.; Wang, Q.; Zhang, G. Y. Fabrication of a thermostable Ga-face GaN template on a molybdenum substrate via layer transfer. *Opt. Mater. Express* **2020**, *10*, 2447–2455.
- (16) Kawan, A.; Yu, S. J. Laser Lift-Off of the Sapphire Substrate for Fabricating Through-AlN-Via Wafer Bonded Absorption Layer Removed Thin Film Ultraviolet Flip Chip LED. *Trans. Electr. Electron. Mater.* **2021**, *22*, 128–132.
- (17) Chen, Y.; Shi, Z. M.; Zhang, S. L.; Ben, J. W.; Jiang, K.; Zang, H.; Jia, Y. P.; Lü, W.; Li, D. B.; Sun, X. J. The van der Waals Epitaxy of High-Quality N-Polar Gallium Nitride for High-Response Ultraviolet Photodetectors with Polarization Electric Field Modulation. *Adv. Electron. Mater.* **2022**, *8*, 2100759.
- (18) Feng, Y. X.; Yang, X. L.; Zhang, Z. H.; Kang, D.; Zhang, J.; Liu, K. H.; Li, X. Z.; Shen, J. F.; Liu, F.; Wang, T.; Ji, P. F.; Xu, F. J.; Tang, N.; Yu, T. J.; Wang, X. Q.; Yu, D. P.; Ge, W. K.; Shen, B. Epitaxy of Single-Crystalline GaN Film on CMOS-Compatible Si(100) Substrate Buffered by Graphene. *Adv. Funct. Mater.* **2019**, *29*, 1905056.
- (19) Zhang, L.; Li, X. L.; Shao, Y. L.; Yu, J. X.; Wu, Y. Z.; Hao, X. P.; Yin, Z. M.; Dai, Y. B.; Tian, Y.; Huo, Q.; Shen, Y. N.; Hua, Z.; Zhang, B. G. Improving the Quality of GaN Crystals by Using Graphene or Hexagonal Boron Nitride Nanosheets Substrate. *ACS Appl. Mater. Interfaces* **2015**, *7*, 4504–4510.
- (20) Ning, J.; Yan, C. C.; Jia, Y. Q.; Wang, B. Y.; Zeng, Y.; Zhang, J. C.; Wang, D.; Hao, Y. GaN Films Deposited on Sapphire Substrates Sputter-Coated with AlN Followed by Monolayer Graphene for Solid-State Lighting. *ACS Appl. Nano Mater.* **2020**, *3*, 5061–5069.
- (21) Chen, Y.; Zang, H.; Jiang, K.; Ben, J. W.; Zhang, S. L.; Shi, Z. M.; Jia, Y. P.; Lü, W.; Sun, X. J.; Li, D. B. Improved nucleation of AlN on in situ nitrogen doped graphene for GaN quasi-van der Waals epitaxy. *Appl. Phys. Lett.* **2020**, *117*, 051601.
- (22) Chen, Y.; Zhang, N.; Li, Y.-F.; Bi, Y.-G.; Yue, Y.-Y.; Feng, J.; Sun, H.-B. Microscale-Patterned Graphene Electrodes for Organic Light-Emitting Devices by a Simple Patterning Strategy. *Adv. Optical Mater.* **2018**, *6*, 1701348.
- (23) Suk, J. W.; Kitt, A.; Magnuson, C. W.; Hao, Y. F.; Ahmed, S.; An, J.; Swan, A. K.; Goldberg, B. B.; Ruoff, R. S. Transfer of CVD-Grown Monolayer Graphene onto Arbitrary Substrates. *ACS Nano* **2011**, *5*, 6916–6924.
- (24) Achra, S.; Wu, X. Y.; Trepalin, V.; Nuytten, T.; Ludwig, J.; Afanas'ev, V.; Brems, S.; Sorée, B.; Tokei, Z.; Heyns, M.; Asselberghs, I. Metal induced charge transfer doping in graphene-ruthenium hybrid interconnects. *Carbon* **2021**, *183*, 999–1011.
- (25) Yamada, K.; Asahi, H.; Tampo, H.; Imanishi, Y.; Ohnishi, K.; Asami, K. Strong photoluminescence emission from polycrystalline GaN layers grown on W, Mo, Ta, and Nb metal substrates. *Appl. Phys. Lett.* **2001**, *78*, 2849–2851.
- (26) Ben, J. W.; Shi, Z. M.; Zang, H.; Sun, X. J.; Liu, X. K.; Lü, W.; Li, D. B. The formation mechanism of voids in physical vapor deposited AlN epilayer during high temperature annealing. *Appl. Phys. Lett.* **2020**, *116*, 251601.
- (27) Chen, Z. L.; Zhang, X.; Dou, Z. P.; Wei, T. B.; Liu, Z. Q.; Qi, Y.; Ci, H. N.; Wang, Y. Y.; Li, Y.; Chang, H. L.; Yan, J. C.; Yang, S. Y.; Zhang, Y. F.; Wang, J. X.; Gao, P.; Li, J. M.; Liu, Z. F. High-Brightness Blue Light-Emitting Diodes Enabled by a Directly Grown Graphene Buffer Layer. *Adv. Mater.* **2018**, *30*, 1801608.
- (28) Jindal, V.; Shahedipour-Sandvik, F. Density functional theoretical study of surface structure and adatom kinetics for wurtzite AlN. *J. Appl. Phys.* **2009**, *105*, 084902.
- (29) Escorcía-Salas, G. E.; Rivera-Julio, J.; López-Pérez, W.; González-Hernández, R.; Sierra-Ortega, J. Interface structural stability of Zr on the AlN(0001) surface: An ab-initio study. *Phys. Status Solidi B* **2013**, *250*, 1526–1531.
- (30) Chen, Y.; Jiang, K.; Zang, H.; Ben, J. W.; Zhang, S. L.; Shi, Z. M.; Jia, Y. P.; Lü, W.; Li, D. B.; Sun, X. J. Growth of high-quality wafer-scale graphene on dielectric substrate for high-response ultraviolet photodetector. *Carbon* **2021**, *175*, 155–163.
- (31) Chen, Y.; Wu, Y.; Ben, J. W.; Jiang, K.; Jia, Y. P.; Zhang, S. L.; Zang, H.; Shi, Z. M.; Duan, B.; Sun, X. J.; Li, D. B. A high-response ultraviolet photodetector by integrating GaN nanoparticles with graphene. *J. Alloys Compd.* **2021**, *868*, 159281.
- (32) Xiao, H. B.; Lo, S.-C.; Tai, Y.-H.; Ho, Y.-L.; Clark, J. K.; Wei, P.-K.; Delaunay, J.-J. Spectrally selective photodetection in the near-infrared with a gold grating-based hot electron structure. *Appl. Phys. Lett.* **2020**, *116*, 161103.
- (33) Hanzaz, M.; Bouhdada, A.; Gibart, P.; Omnès, F. Impact of the defects on the electrical and optical properties of AlGaN ultraviolet photodetectors. *J. Appl. Phys.* **2002**, *92*, 13–18.
- (34) Perdew, J. P.; Burke, K.; Ernzerhof, M. Generalized Gradient Approximation Made Simple. *Phys. Rev. Lett.* **1996**, *77*, 3865–3868.
- (35) Kresse, G.; Furthmüller, J. Efficient iterative schemes for ab initio total-energy calculations using a plane-wave basis set. *Phys. Rev. B* **1996**, *54*, 11169–11186.
- (36) Kresse, G.; Furthmüller, J. Efficiency of ab-initio total energy calculations for metals and semiconductors using a plane-wave basis set. *Comput. Mater. Sci.* **1996**, *6*, 15–50.
- (37) Kresse, G.; Joubert, D. From ultrasoft pseudopotentials to the projector augmented-wave method. *Phys. Rev. B* **1999**, *59*, 1758–1775.
- (38) Henkelman, G.; Uberuaga, B. P.; Jónsson, H. A climbing image nudged elastic band method for finding saddle points and minimum energy paths. *J. Chem. Phys.* **2000**, *113*, 9901–9904.

Recommended by ACS

Preparation and Structural Investigation of Ultra-Uniform Mo Films on a Si/SiO₂ Wafer by the Direct-Current Magnetron Sputtering Method

Zhengwang Cheng, Xinguo Ma, *et al.*

JANUARY 09, 2023
CRYSTAL GROWTH & DESIGN

READ 

Modeling-Based Design of the Control Pattern for Uniform Macrostep Morphology in Solution Growth of SiC

Yifan Dang, Toru Ujihara, *et al.*

JANUARY 05, 2023
CRYSTAL GROWTH & DESIGN

READ 

Formation and Increased Photoelectrochemical Properties of Free-Standing Nanoporous GaN-Based MQW Photoanodes Embedded on Nanoporous GaN Reflectors

Dezhong Cao, Xiaohua Ma, *et al.*

JANUARY 30, 2023
CRYSTAL GROWTH & DESIGN

READ 

Polarity Control by Inversion Domain Suppression in N-Polar III-Nitride Heterostructures

Hengfang Zhang, Vanya Darakchieva, *et al.*

JANUARY 19, 2023
CRYSTAL GROWTH & DESIGN

READ 

Get More Suggestions >